Biosensors and Bioelectronics 131 (2019) 9–16

Contents lists available at ScienceDirect

Biosensors and Bioelectronics

journal homepage: www.elsevier.com/locate/bios

Three-dimensional drivable optrode array for high-resolution neural stimulations and recordings in multiple brain regions

Ming-Hao Wang[a], Xiao-Wei Gu[b,c], Bo-Wen Ji[a], Long-Chun Wang[a], Zhe-Jun Guo[a], Bin Yang[a], Xiao-Lin Wang[a], Cheng-Yu Li[b,c], Jing-Quan Liu[a,*]

[a] National Key Laboratory of Science and Technology on Micro/Nano Fabrication Laboratory, Key Laboratory for Thin Film and Microfabrication of the Ministry of Education, Collaborative Innovation Center of IFSA, Department of Micro/Nano-electronics, Shanghai Jiao Tong University, Shanghai 200240, PR China
[b] Institute of Neuroscience and Key Laboratory of Primate Neurobiology, Shanghai Institutes for Biological Sciences, Chinese Academy of Sciences, Shanghai 200031, PR China
[c] University of Chinese Academy of Sciences, Peking, PR China

ARTICLE INFO

Keywords:
Optrode array
3-dimensional integration
Neural recording
Optical stimulation
Laser diode

ABSTRACT

The brain-computer interface (BCI) devices are of prime important for study of nervous system as well as diagnosis and treatment of neurological disorders. To meet the needs of the BCI devices in high-density integration and multi-functionalization, 3-dimensional (3D) drivable optrode array with laser diodes (LDs) coupled waveguides was developed. The unique device realizes the 3D integration of the optrodes and avoids fiber tangle and tissue heating by adopting LD coupled waveguide structure. Besides, the postoperative position adjustment of the optrode array was achieved by integrating with a 3D printed micro-drive. Most importantly, high-resolution neural stimulations and recordings were achieved for study of working memory related neural circuits in four brain regions of mice including prelimbic cortex (PrL), mediodorsal thalamic nucleus (MD), dorsal medial caudate nucleus (dmCP) and posterior motor cortex 2 (pM2). The results indicate that this novel device is promising for the research of complex neural networks.

1. Introduction

Neural circuits are intricately linked in the brain and govern complex signal pathways responsible for thought, memory, emotion and behavior (Kampasi et al., 2016). In general, the dynamic relations between neural pathways can be studied by functional electrical stimulation and electrophysiological recording of neurons in specific regions. For this purpose, a variety of neural probes based on micro-wire electrodes (Liao et al., 2011; Xie et al., 2016; Ferguson et al., 2009) carbon fiber electrodes (Patel et al., 2015, 2016; Guitchounts et al., 2013) and micromachined electrodes (Wise et al., 1970; Najafi et al., 1985; Kewley et al., 1997; Norlin et al., 2002) have been developed and extensively applied in the past decades. However, electrical stimulation offers insufficient spatial resolution and lacks cell-type specificity. Meanwhile, the high current densities required for an effective stimulation bear the risk of causing damage to the electrode-tissue interface (Butterwick et al., 2007). With the advent of optogenetics (Boyden et al., 2005; Deisseroth, 2013; Madisen et al., 2012; Zemelman et al., 2002; Nagel et al., 2003) it is now possible to directly activate and inhibit neural activities at high spatial and temporal resolution (Yizhar et al., 2011; Häusser, 2014; Miesenböck, 2011).

Optogenetics is based on the genetic transfection of specific cell types to express photosensitive proteins (called opsins), which can be controlled by wavelength-specific light. Opsins display a wide range of spectral sensitivity and can be used to activate (depolarize) or silence (hyperpolarize) the targeted neurons. For example, Channelrhodopsin-2 (ChR2) responds to ~470 nm light and depolarizes the targeted cells (Nagel et al., 2005). Other opsins like Archaerhodopsin (Arch) (Chow et al., 2010; Han et al., 2011) and Halorhodopsins (NpHr) (Han and Boyden, 2007; Zhang et al., 2007), respond to ~590 nm light and hyperpolarize the targeted cells. Although the number of opsins is increasing (Govorunova et al., 2015; Klapoetke et al., 2014; Wietek et al., 2015), technology that can realize high-resolution neural stimulations and recordings from multiple brain regions in behaving animals is not yet available. The conventional approach utilizes a micro-wire electrode array integrated with an optic fiber (Adamantidis et al., 2007; Aravanis et al., 2007), which can manipulate neural activity in regions where opsins have been expressed. It is challenging to deliver light through a fiber with high spatial resolution. Other approaches include multipoint-emitting optic fibres (Pisanello et al., 2014; Lee et al., 2015),

* Corresponding author.
E-mail address: jqliu@sjtu.edu.cn (J.-Q. Liu).

https://doi.org/10.1016/j.bios.2019.01.019
Received 1 November 2018; Received in revised form 28 December 2018; Accepted 14 January 2019
Available online 05 February 2019
0956-5663/

monolithically integrated dielectric waveguides (Wu et al., 2013) and three-dimensional multi-waveguide probes (Zorzos et al., 2012). However, they employ expensive and bulky light sources which become an issue as they are scaled up to multiple stimulation regions. Recently, the silicon-based microelectrode integrated with LDs coupled waveguides have been demonstrated enable activation and silencing of the same or different groups of neurons while simultaneously recording from them (Kampasi et al., 2018; Schwaerzle et al., 2013, 2017). These devices directly utilize the assembled micro LDs as light sources to avoid the fiber tangle. The spatial resolution and scalability of the optrodes can be dramatically improved by this technology. However, the optrodes typically have a few two-dimensional shanks, which allows them to record or stimulate neurons only in a single brain region. Besides, the reported optrodes are mostly bonded to printed circuit board (PCB) and then attached to the skull, which make it impossible to adjust their positions after in-vivo implantation.

In this paper, we described the design and in-vivo use of a novel 3D drivable optrode array with LDs coupled waveguides. The key design elements of this optrode array are the optoelectron integration and the 3D assembly of the optrodes based on anisotropic conductive adhesive (ACF). Furthermore, high-resolution neural manipulation and flexible postoperative position adjustment of this optrode array were achieved in multiple brain regions of mice. To the best of our knowledge, the design and in-vivo use of this novel 3D drivable optrode array with LDs coupled waveguides has rarely been reported.

2. Materials and methods

2.1. Optrodes fabrication

Fig. S1 showed the fabrication process of the optrodes. At first, a silicon-on-insulator (SOI) wafer was chosen as the substrate. The thickness of the silicon device layer, the buried oxide layer and the handle layer of the SOI wafer were 30 μm, 2 μm and 450 μm respectively. After washed in ultrasonic bath and dried in oven, 1 μm thick of silicon oxide was deposited on the device layer by Plasma Enhanced Chemical Vapor Deposition (PECVD) system to form the bottom dielectric layer. This oxide layer has compressive stress which compensated the tensile stresses from the thick SU-8 layers that will be patterned later for the waveguide. Then the Cr/Au layers (30/300 nm) were sputtered and patterned to form the electrode sites, conductive traces and bonding pads. After that, another 2 μm thick of silicon oxide was deposited by PECVD to form the top dielectric layer. The oxide layer on the electrode sites, trenches and bonding pads were removed by Reactive Ion Etching (RIE). The front release lines of the optrodes were defined by RIE of the oxide layer and Deep Reactive Ion Etching (DRIE) of the silicon device layer. After that, a layer of 15 μm thick SU-8 was spin-coated and patterned on the oxide layer to form the waveguide. The fabrication of SU-8 waveguide can only be done after all the RIE and DRIE processes were completed. It was because the removing of photoresist after RIE/DRIE was difficult and may lead to the damage of the surface structure of SU-8 waveguide. The oxide layer on the back side of the wafer were patterned by double-sided lithography and RIE and then served as hard mask of the back side DRIE. Finally, the buried oxide was cleaned by RIE and the wafer was put into acetone to release the optrodes from the substrate.

2.2. Electrochemical deposition and characterization

The optrodes were modified with platinum black (Pt-Black) to improve the electrochemical performance. The Pt-Black coatings were electroplated by applying repetitive current pulses (duty ratio of 5 ms: 500 ms, peak current density of 4.5 A/cm^2, cycles of 240) in chloroplatinic acid solution (3% chloroplatinic acid and 0.01% lead acetate in deionized water, lead ions have been shown to increase the adherence of Pt black on the substrate) under ultrasonication. The current pulses were generated by an electrochemical workstation (CHI660C, CH instrument) with a gold rod as the reference and counter electrode. The electrochemical impedance spectrum (EIS) was measured by Autolab (PGSTAT204, Switzerland) in phosphate buffered saline (PBS, pH 7.4) with saturated calomel electrode (SCE) as the reference electrode and a Pt foil as the counter electrode. EIS was measured at frequency range from 0.1 Hz to 100,000 Hz with input voltage amplitude of 0.01 V.

2.3. Chronic implantation of the optrode array

Chronic recording and stimulation were performed on male Thy1-ChR2-YFP (Jackson Labs 07615). All animal studies and experimental procedures were approved by the Animal Care and Use Committee of the Institute of Neuroscience, Chinese Academy of Sciences, Shanghai, China. Mice were anaesthetized by isoflurane and fixed on stereotaxic frame before surgery. Scalp and other associated soft tissue were removed and the exposed skull was cleaned by 3% hydrogen peroxide solution and filtered artificial cerebrospinal fluid (ACSF). After that, a layer of tissue adhesive (Kwik-Sil) was applied on the surface of the skull. A steel plate was placed on the skull and then fixed by dental cement. Then the mice were attached to the stereotaxic frame by the steel plate and craniotomies of ~2 × 4 mm^2 were made above the four brain regions. Dura mater was carefully removed with surgery needles with as less bleeding as possible. The center of the optrode array was targeted to AP 2.00 mm, ML 0.40 mm and DV 1.65 mm for PrL, AP 0.86 mm, ML 0.50 mm and DV 0.50 mm for pM2, AP 0.86 mm, ML 1.20 mm and DV 2.50 mm for dmCP and AP + 0.86 mm, ML 0.50 mm, DV 0.50 mm for MD. After that, the micro-drive was fixed on the metal plate by tissue gel and dental cement for the chronic implantation.

2.4. Neural recordings and signals analysis

Recorded neural signals were acquired using a Multi-channel Neural Acquisition Processor (Plexon Inc, Dallas, TX). Neural electrophysiological signals were amplified and band-pass filtered. Action potential recordings were sampled at 40 kHz and band-pass filtered from 250 to 8000 Hz, while local field potentials were band-pass filtered from 0.5 to 250 Hz. During recording sessions, animals were placed in an electrically shielded recording box and continuous neural recording was taken. Offline spike detection was performed with Offline Sorter. Typically, negative four/five times of standard deviation of recorded signals were set as thresholds for detecting spike events. Signal amplitude for a cluster was defined as the averaged peak-to-peak amplitude of each cluster. The root-mean-square (RMS) noise voltage for the recording sites in each recorded segment was calculated after all spike waveforms had been removed. The signal-to-noise ratio (SNR) for a given cluster was defined as follows:

$$\text{SNR} = \text{Signal Amplitude}/(2 \times \text{Averaged RMS Noise Voltage})$$

3. Results and discussion

3.1. Design and fabrication of the 3D drivable optrode array

The schematic diagram of the assembled 3D drivable optrode array was shown in Fig. 1. Overall, the device was composed of three parallelly stacked optrodes, a 3D printed micro-drive and three Omnetics connectors. The optrodes were fabricated on a SOI wafer by using micromaching technology (Fig. S1). After released from the wafer, the optrodes were integrated with blue-light LDs (445 nm, 80 mW) for photoelectron integration. As illustrated in Fig. 1D, the anode of the LD was bonded on the optrode by ACF-bonding and the cathode of the LD was bonded by wire-bonding. In order to prevent the overflowed ACF blocking the light-emitting window of the LD, a releasing trench was designed between the waveguide and the bonding pad. The releasing

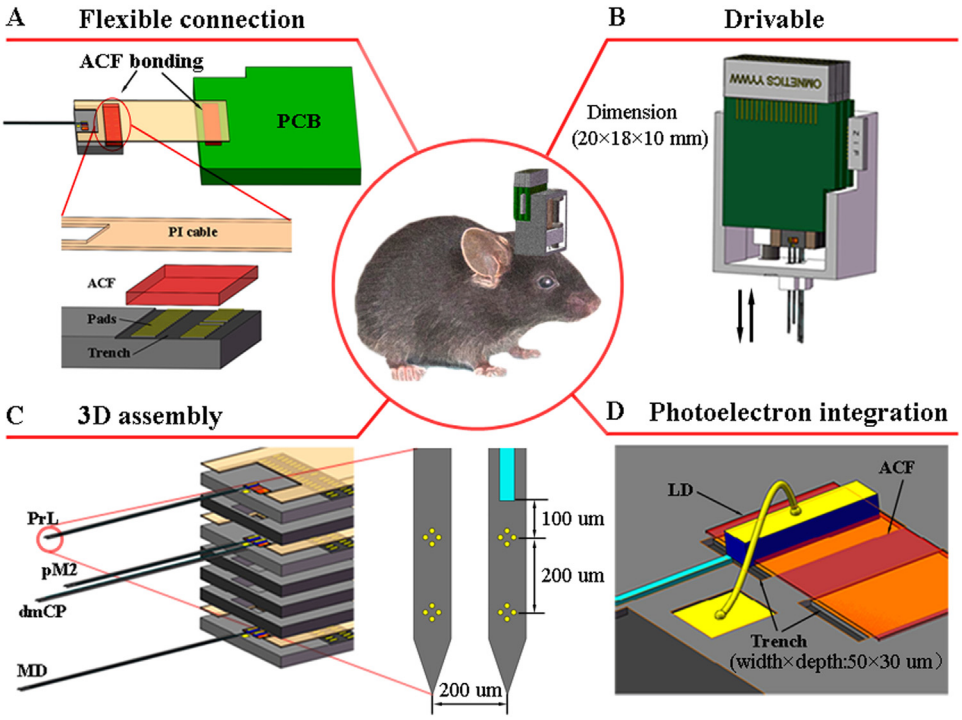

Fig. 1. The design of the 3D drivable optrode array. (A) The schematic diagram of the optrode bonded to a flexible cable connecting with a PCB. (B) The schematic diagram of the optrode integrated with a micro-drive. (C) The explosive view of the 3D stacked optrode array. (D) The schematic diagram of a LD bonded on the base of the optrode.

trench had a width of 50 μm and depth of 30 μm. The optrode was bonded with a flexibe polyimide (PI) cable to transfer the signals between the optrode and the connector (Fig. 1A). The bonding method of the optrode with the flexible cable had been described in our previous work (Wang et al., 2018). The unique of this method is the structural design of the trench encircled bonding pad as shown in the inset of Fig. 1A. The structure makes the pads becoming bumped spots which are necessary for ACF-bonding. Therefore, the bonding of the optrode with the cable can be done directly without plating metal bumping on the pads. After that, three optrodes were stacked together for 3D integration as shown in Fig. 1C. By using some spacers to adjust the vertical spacing between the optrodes, the shanks can be precisely inserted into the corresponding brain regions, respectively. As can be seen, there are two shanks with one waveguide and sixteen electrodes located in each brain region. The electrodes are distributed as four tetrodes with an interval of 200 μm and the pitch between the neighboring electrodes is 31 μm. The distance between the waveguide and the tetrode is 100 μm. Therefore, high-resolution neural stimulations and recordings can be realized in mice brains. Finally, the optrode array was assembled with a 3D printed micro-drive for in-vivo implantation (Fig. 1B). As the optrode array was floatingly fixed on the micro-drive, the recording and stimulating position can be precisely controlled by the driving screw.

The detailed photoelectron integration and 3D assembly processes were described in Fig. 2. For photoelectron integration, LDs were bonded on optrodes with the aid of ACF-bonding and wire-bonding as illustrated in Fig. 2**A**. Firstly, a layer of ACF was applied on the pad of the optrode and the lamination was conducted on a hot-press machine for primary fixation of ACF. After removing the releasing film from ACF, the optrode was fixed on the stage of an ultrasonic wire-bonding machine and the temperature of the stage was raised to 210 °C to melt the epoxy in ACF. Then, an LD was picked up by the cleaver of the wire-bonding machine and transferred to the bonding pad. After aligned to the waveguide by micromanipulator, the LD was attached on the ACF-covered bonding pad and the temperature of the stage was cooled down to room temperature for solidification. After the ACF-bonding, the top pad of the LD was bonded with the pad of the optrode by wire-bonding. Fig. 2B showed the optical micrograph of a LD bonded on the optrode. As can be seen, the LD was aligned to the waveguide accurately and attached to the bonding pad tightly. The dimension of the LD is 90 × 150 × 600 μm^3 (thickness × width × length). The waveguide had a thickness of 15 μm and width of 30 μm. For 3D integration, three optrodes with different structures were stacked together by using epoxy as adhesive layer and micromachined spacers as interlayers (Fig. 1C). The spacers were fabricated on a silicon wafer which had a thickness equal to the minimal stacking interval. Besides, a cavity structure was designed on the spacer to protect the LD and avoid the light leakage. In order to realize the accurate alignment of the optrodes, a 3D printed mould was used to assist the stacking as illustrated in Fig. 2C. Finally, the fabricated optrode array was fixed on a 3D printed micro-drive which was mainly composed of a case, a slider and a screw (Fig. S3). The optrode array was glued on the slider with their shanks inserted into the bottom tube of the micro-drive. When the screw was twisted, the optrode array will move along with the slider. Thus, the depth of the optrode array can be controlled for accurate positioning in the targeted brain regions. The micrograph of the shanks (Fig. 2D) showed the optrodes were stacked in parallel. The total weight of the 3D drivable optrode array is 4.5 g and the dimension of the device is 20 mm × 18 mm × 10 mm.

3.2. Electrochemical characterization and modification of the optrode array

The performance of electrophysiological signal recording seriously depended on the electrochemical properties of the microelectrodes. Therefore, the assembled optrodes were modified with platinum black (Pt-black) to improve their electrochemical performance. Before that, cyclic voltammetry (CV) and EIS tests were conducted in phosphate buffered saline (PBS, pH 7.4) to check the conductivity of the optrodes. Then, the conductive channels were connected in series for Pt-black deposition. The optical micrograph of the Pt-black modified electrodes was showed in Fig. 3A. As can be seen, Pt-black was coated on the gold electrodes (121 μm^2) uniformly. The scanning electron micrograph (SEM) illustrated the Pt-black was composed of many cauliflower shape particles which attached on the substrate tightly. The EIS of the bare gold electrodes and the Pt-black modified electrodes were measured in-vitro and in-vivo as shown in Fig. 3C. The EIS curves illustrated the

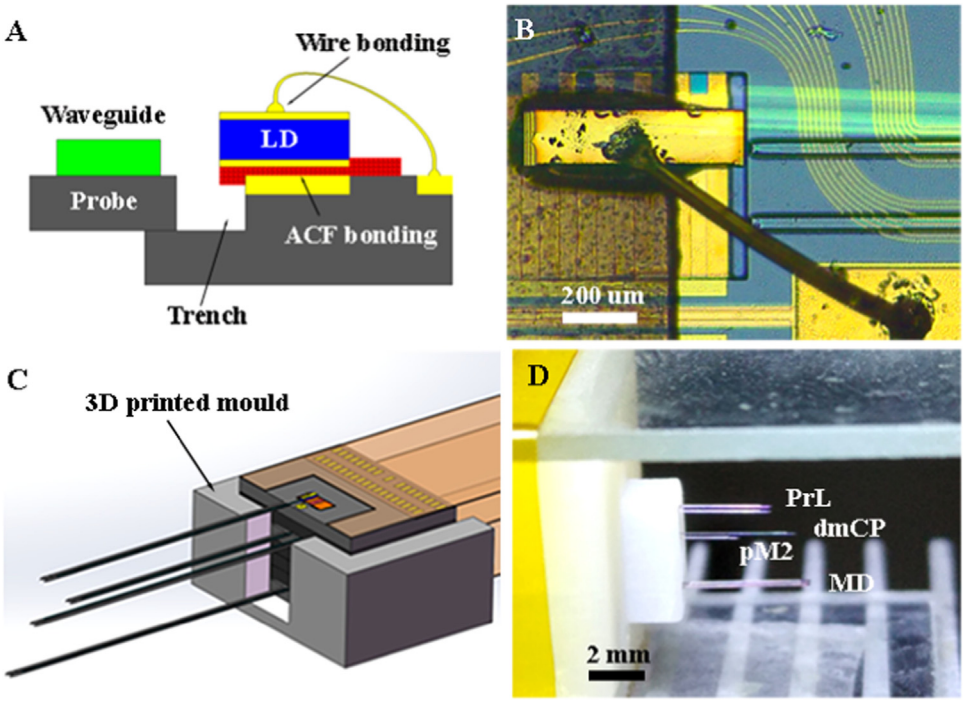

Fig. 2. The detailed photoelectron integration and 3D assembly processes of the drivable optrode array. (A) The ACF-bonding and wire-bonding structure of the LD on the optrode. (B) The optical micrograph of an LD bonded on the optrode. (C) The schematic diagram of the alignment of the 3D optrodes. (D) The micrograph of the shanks inserted in the bottom tube of the micro-drive.

impedance (at 1 kHz) of the bare gold electrode decreased significantly after Pt-black modification which indicated the improved neural recording performance. After in-vivo implantation, the impedance of the Pt-black modified electrode increased from 75.1 kΩ to 794.2 kΩ at 1 kHz. This increment may be attributed to immediate protein absorption on the electrode sites coupled with the impedance of neural tissue (Mavoori et al., 2005; Szarowski et al., 2003). Fig. 3D showed the in-vivo impedance variation of the Pt-black modified electrode over the implantation time. As can be seen, the impedance decreased distinctly in the first two or three days and then increased slowly in the following days. According to relevant literature reports (Winslow and Tresco, 2010; Williams et al., 2007), there are two major tissue reactions that can affect the impedance of electrodes within one week after electrode implantation. One is the swelling of brain tissue caused by surgery, and the other is the glial reaction caused by electrode implantation. The swelling of brain tissue gradually decreases within 3–6 days after implantation, which results in reduced interfacial impedance between electrodes and tissue. However, extensive glial reactions occur at 4th day after implantation, which in turn leads to increased interfacial impedance. Therefore, the decline in the impedance is due to the decrease of the swelling and the increment can be explained by the glial reactions of the brain to the implanted electrode over time.

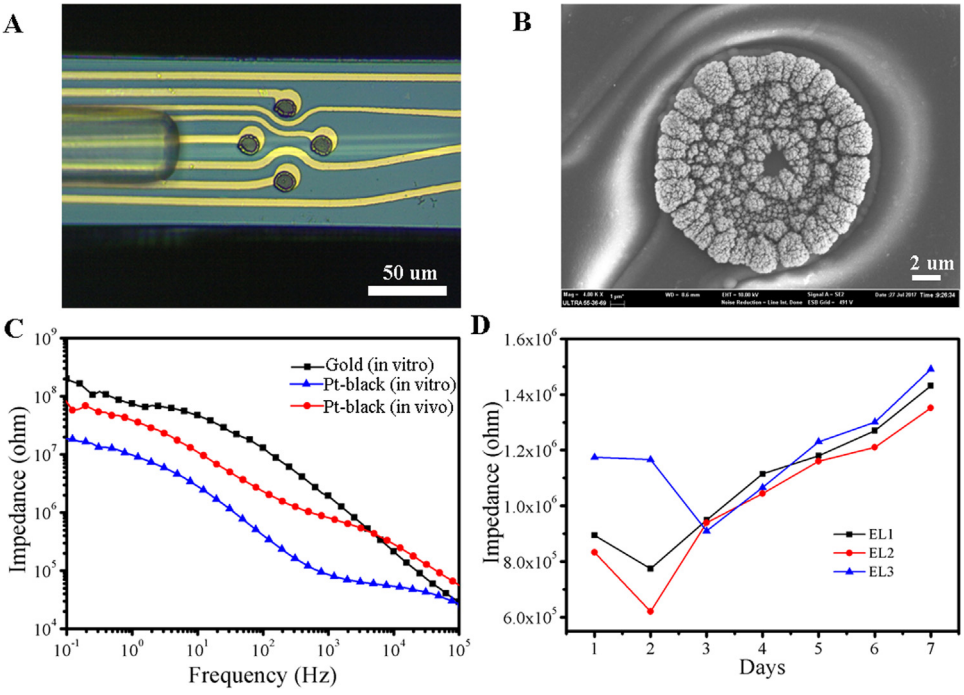

Fig. 3. The electrochemical modification and characterization of the optrode array. (A,B) The optical micrograph and the SEM of the Pt-black modified electrodes. (C) The in-vitro EIS of the bare gold electrode and the in-vitro and in-vivo EIS of the Pt-black modified electrode. (D) The in-vivo impedance variation of the Pt-black modified electrode over the implantation time.

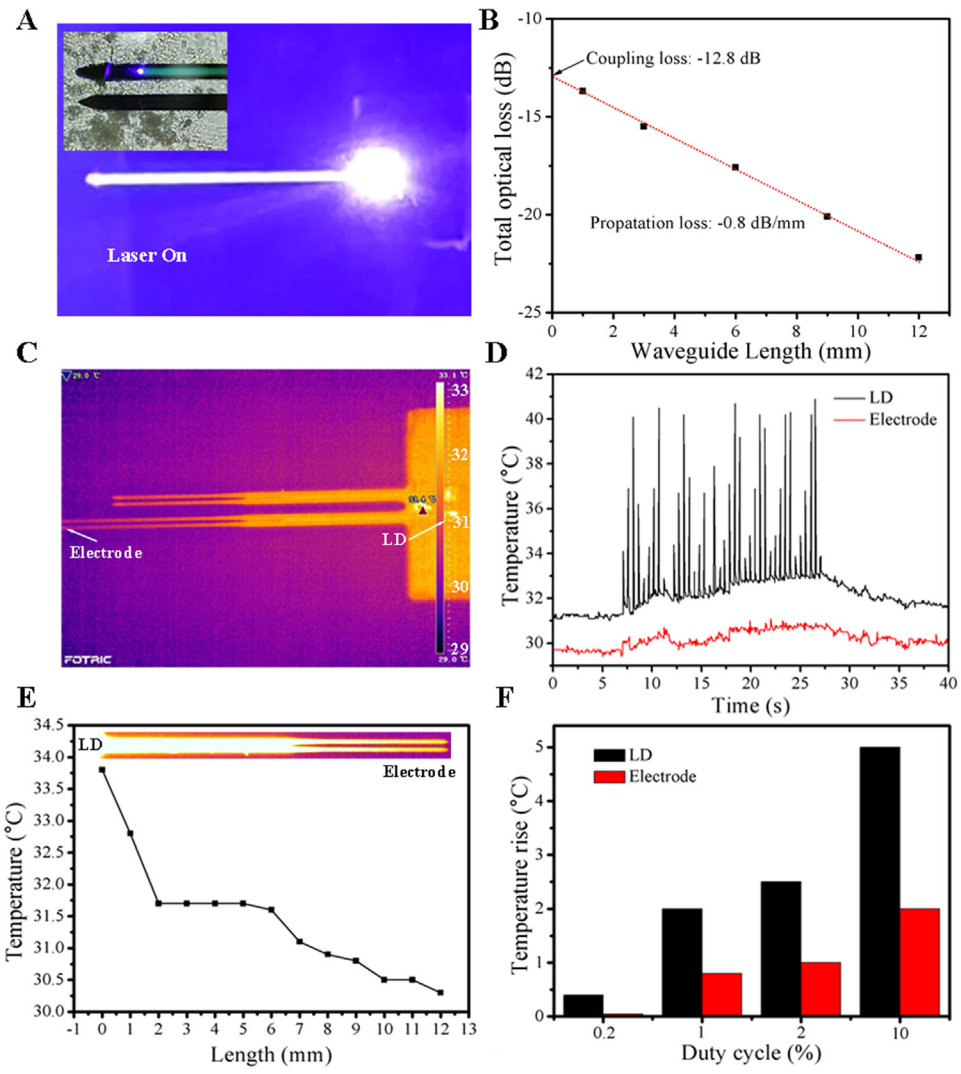

Fig. 4. The optical and thermal characterization of the optrode array. (A) The photo of an optrode with the LD was lighted and the inset showed the dark field micrograph of the waveguide end. (B) The total optical loss measured for different lengths of SU-8 waveguide. (C) The thermal image of an optrode after applying an LD current of 100 mA at DC of 1% and frequency of 10 Hz. (D) The transient thermal responses at two measure spots (LD and electrode), with the LD switched on for about 20 s (E) The temperature distribution of the optrode along the axis of the shanks after the LD switched on for about 20 s (F) The variation of the maximal temperature rise with the DC when the LD current was set as 100 mA.

3.3. Optical and thermal characterization of the optrode array

The optical characterization includes the radiance, propagation loss and coupling loss of the optrode. For this purpose, the LDs were operated at a current of 100 mA, a duty cycle (DC) of 1% and a pulse frequency of 10 Hz. Fig. 4A showed the photo of an optrode with the lighted LD and the inset showed the dark field micrograph of the waveguide end. As can be seen, the laser was coupled into the waveguide and emitted from the end faced clearly. The time-averaged power of the laser emitted from the LD and the waveguide was measured by a photoelectric detector. The results showed the power emitted from the LD was about 197.4 μW and the power emitted from the waveguide (length of 11.6 mm) was about 1.1 μW. As the radiance of waveguide is equal to the radiant power divided by the area of the waveguide end facet, the calculated radiance of this optrode is 2.4 mW/mm^2. This value is enough to activate ChR2-expressed neurons. In this optrode, the coupling loss (between the LD and the SU-8 waveguide) and the propagation loss (through the SU-8 waveguide) are the two main sources of the total optical loss. Thus, a cutback method was used to estimate the coupling and propagation loss. Specifically, a testing structure consisted of straight SU-8 waveguide with different lengths was fabricated and the output power at the end of each waveguide was measured (Fig. 4B). Based on these measurements, the propagation loss was estimated at − 0.8 dB/mm by computing the slope and the coupling loss at − 12.8 dB by finding the y-intercept through extrapolation. This propagation loss was mainly due to natural attenuation in SU-8 which depends highly on the wavelength (Son et al., 2015).

Since the optrode contains active optoelectronic components, temperature rise of the optrode has to be quantified in view of the safe operation of this device. The ISO 14708-1 standard for active implantable medical devices defines a general limit of temperature rise $\Delta T = 2$ K for the outer surface of an implanted device with respect to the surrounding body temperature of 37 °C. To verify whether the optrode operates within these limits, we measured ΔT by a high-resolution infrared camera (Fotric 228s, USA). The measurement was performed with an optrode assembled to a glass slide and its shanks floating in air. This measurement configuration represents the worst case for ΔT on the shank, since the thermal coupling of the shanks to air is less effective than that to tissue. The thermal image in Fig. 4C was taken after applying an LD current of 100 mA at DC of 1% and frequency of 10 Hz. The temperature rise of the entire probe was clearly visible. Transient thermal responses at two measure spots (LD and electrode), with the LD switched on for about 20 s, were shown in Fig. 4D. As can be seen, the measured ΔT of LD and electrode was about 10 K and 1 K, respectively. The results indicated this operation was safe for in-vivo optical stimulation. The temperature distribution of the optrode along the axis of the shanks after the LD switched on for about 20 s was shown in Fig. 4E. The temperature decreases rapidly in the front 2 mm is due to the high temperature grad. It stays steady in the range of 2–6 mm because of the high thermal conductivity of the substrate (the shank in this range was not thinned). The temperature in the range of 6–12 mm was slowly decreased because the shank was thinned to 30 μm, which was

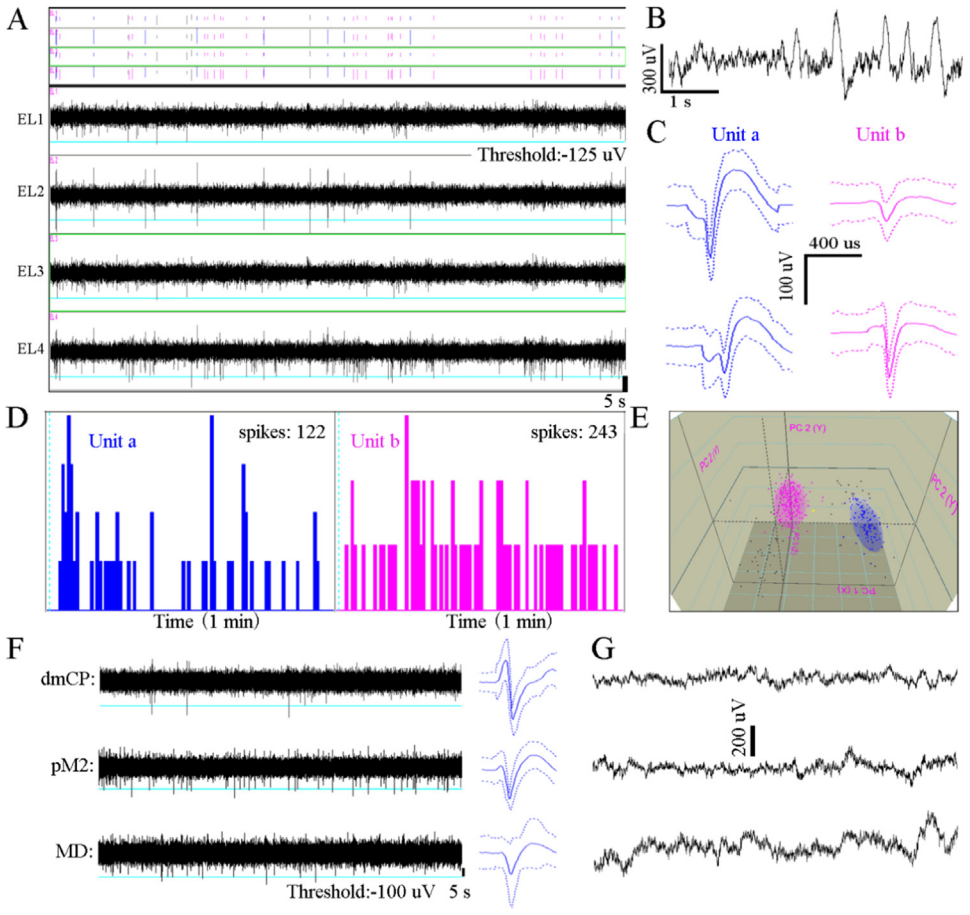

Fig. 5. The spontaneous neural recordings of the optrode array implanted in mouse brain. The recorded (A) spontaneous APs and (B) LFPs from one tetrode of the optrode implanted in PrL. (C) The waveforms of two units sorted from channel EL2 and EL4. (D) The firing events of the two sorted units during one minute of recording. (E) The PCA of the two sorted units. The (F) APs and (G) LFPs signals recorded from dmCP, pM2 and MD.

beneficial to heat dissipation. Fig. 4F showed the variation of the maximal temperature rise with the DC when the LD current was set as 100 mA. It indicated that the temperature rise of the optrode increased with DC and the upper limit of the DC for safe optical stimulation is 10% when the frequency is 10 Hz.

3.4. *In-vivo neural recording and optical stimulation with the optrode array*

To demonstrate the neural recording capacity of the 3D drivable optrode array in multiple brain regions, spontaneous action potentials (APs) and local field potentials (LFPs) were recorded after electrode implantation in PrL, MD, dmCP and pM2 for one week. The PrL has been proved to be involved in the working memory related activity (Fuster and Alexander, 1971; Liu et al., 2014). Meanwhile, the MD, dmCP, pM2 are downstream brain regions of PrL (Oh et al., 2014) and they also participate in the working memory related activity (Churchland et al., 2010; Pasupathy and Miller, 2005; Watanabe and Funahashi, 2004). Therefore, these four brain regions were selected to research the working memory related neural circuit. As shown in Fig. 5A, spontaneous action potentials can be recorded clearly from one tetrode of the optrode array implanted in PrL. The corresponding LFP signal was shown in Fig. 5B. It was easy to see, the baseline of the LFP signal was stable and the amplitude was about 400 μV. Fig. 5C illustrated the waveforms of two sorted units from channel EL2 and EL4. As can be seen, the amplitude of "unit a" recorded from channel EL2 is larger than that recorded from channel EL4 and the amplitude of "unit b" recorded from the two channels was exactly opposite to that of the former. The amplitude of the two units indicated the position of "unit a" is closer to EL2 and the position of "unit b" was closer to EL4. The firing events of the two sorted units during one minute of recording were exhibited in Fig. 5D. The results showed the total spikes of "unit a" and "unit b" were 122 and 243 and the corresponding firing rate was about 2 Hz and 4 Hz, respectively. Fig. 5E showed the principal component analysis (PCA) of the two sorted units. The APs and LFPs signals recorded from dmCP, pM2 and MD were illustrated in Fig. 5F,G. As can be seen, single unit recordings can be realized in these brain regions simultaneously. The averaged amplitudes of the APs recorded from dmCP, pM2 and MD were about 138 μV, 105 μV and 80 μV and the averaged RMS noises of this optrode array was about 15.2 μV. Thus, the signal to noise ratio (SNR) of this optrode array was in the range of 2.63–4.54. The results indicated the high-quality neural recording ability of the 3D drivable optrode array in multiple brain regions of mice.

The neural stimulation capacity of the 3D drivable optrode array was studied by applying a train of laser pulses (10 Hz of frequency, 1% of DC and 100 mA of LD current) in MD and recording the neural activities in PrL simultaneously. The 3D drivable optrode array implanted in a mouse brain was showed in Fig. 6A. The inset illustrated the stimulation and recording regions of the optrode array. Fig. 6B showed the micrograph of the cranial window for electrode implantation and the size of the window is about 2 mm × 4 mm. The neural activities recorded from the optrode implanted in PrL before and after applying a train of laser pulses in MD were exhibited in Fig. 6C. As can be seen, spontaneous action potentials can be recorded clearly in channel EL4 before stimulation. But the firing rate seemed to decreased after the laser pulses were applied. In order to verify the change of firing rate, spike waveforms were detected and sorted by Offline Sorter. Fig. 6D showed the waveforms of one unit sorted from this tetrode. The firing events of this unit during 80 s of recording were shown in Fig. 6E. The statistics indicated that the firing rate of the unit in PrL decreased significantly during the optical stimulation in MD and it returned to normal level after the stimulation was shut down. The reason may be

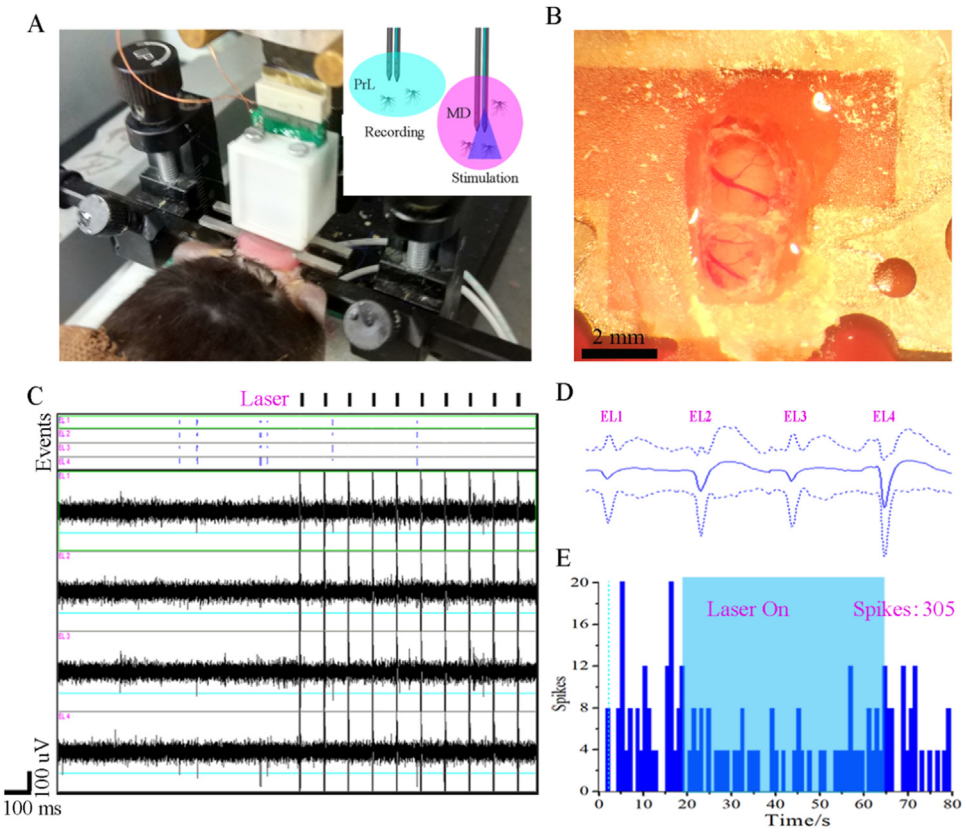

Fig. 6. The optical activated neural recordings of the 3D drivable optrode array. (A) The photo of a 3D drivable optrode array implanted in a mouse brain. The inset illustrated the stimulation and recording regions of the optrode array. (B) The micrograph of the cranial window for electrode implantation. (C) The neural activities recorded from one tetrode of the optrode implanted in PrL before and after applying a train of laser pulses (10 Hz frequency, 1% DC and 100 mA LD current) in MD. (D) The waveforms of one unit sorted from this tetrode. (E) The firing events of this unit during 80 s of recording. The shadow area indicated the range where the laser pulses were applied.

that the laser pulses activated some neurons in MD which had the function to suppress the neural activities in PrL. The results suggested that there may be a working memory related neural circuit between the two brain regions.

4. Conclusions

In conclusion, we developed a novel 3D drivable optrode array with LDs coupled waveguides for high-resolution neural recording and stimulation in multiple brain regions. The optical characterization showed the radiance of this optrode was 2.4 mW/mm^2, which was enough to activate ChR2-expressed neurons. The thermal characterization indicated the temperature rise of the optrode was safe for neural stimulation when the duty cycle of the laser pulses (10 Hz, 100 mA) was less than 10%. The spontaneous neural recording in PrL, MD, dmCP and pM2 showed single-unit recording can be realized by the optrode array and the SNR was in the range of 2.63–4.54. The neural stimulation capacity of the optrode array was studied by applying a train of laser pulses in MD and recording the neural activities in PrL. The statistics indicated the optical stimulation applied in MD can suppress neuron activities in PrL. The results indicate that this novel device is promising for the research of complex neural networks.

CRediT authorship contribution statement

Ming-Hao Wang: Conceptualization, Methodology, Validation, Writing - original draft. **Xiao-Wei Gu:** Conceptualization, Methodology. **Bo-Wen Ji:** Writing - review & editing. **Long-Chun Wang:** Writing - review & editing. **Zhe-Jun Guo:** Writing - review & editing. **Bin Yang:** Writing - review & editing. **Xiao-Lin Wang:** Writing - review & editing. **Cheng-Yu Li:** Supervision, Resources. **Jing-Quan Liu:** Funding acquisition, Writing - review & editing, Project administration.

Acknowledgements

The authors thank to partly financial support from the National Key R&D Program of China under Grant 2017YFB1002501, the National Natural Science Foundation of China (Nos. 51475307 and 61728402), the Research Program of Shanghai Science and Technology Committee (17JC1402800), the Program of Shanghai Academic/Technology Research Leader (18XD1401900). The authors thank to Shanghai Institutes for biological sciences, Chinese Academy of Sciences. The authors are also grateful to the Center for Advanced Electronic Materials and Devices (AEMD) of Shanghai Jiao Tong University.

Declaration of interests

None.

Appendix A. Supplementary material

Supplementary data associated with this article can be found in the online version at doi.org/10.1016/j.bios.2019.01.019.

References

Adamantidis, A.R., Zhang, F., Aravanis, A.M., Deisseroth, K., De Lecea, L., 2007. Nature 450 (7168), 420–424.
Aravanis, A.M., Wang, L.P., Zhang, F., Meltzer, L.A., Mogri, M.Z., Schneider, M.B., 2007. J. Neural Eng. 4 (3), 143.
Boyden, E.S., Zhang, F., Bamberg, E., Nagel, G., Deisseroth, K., 2005. Nat. Neurosci. 8 (9), 1263–1268.
Butterwick, A., Vankov, A., Huie, P., Freyvert, Y., Palanker, D., 2007. IEEE Trans. Bio-Med. Eng. 54 (12), 2261.
Chow, B.Y., Han, X., Dobry, A.S., Qian, X., Chuong, A.S., Li, M., 2010. Nature 463 (7277), 98.
Churchland, M.M., Cunningham, J.P., Kaufman, M.T., Ryu, S.I., Shenoy, K.V., 2010. Neuron 68 (3), 387–400.
Deisseroth, K., 2013. P. Natl. Acad. Sci. USA 110 (41), 16287 (16287).
Ferguson, J.E., Boldt, C., Redish, A.D., 2009. Sens. Actuators A-Phys. 156 (2), 388–393.
Fuster, J.M., Alexander, G.E., 1971. Science 173 (3997), 652–654.
Govorunova, E.G., Sineshchekov, O.A., Janz, R., Liu, X., Spudich, J.L., 2015. Science 349 (6248), 647–650.
Guitchounts, G., Markowitz, J.E., Liberti, W.A., Gardner, T.J., 2013. J. Neural Eng. 10 (4), 046016.
Han, X., Boyden, E.S., 2007. PLoS One 2 (3), 299.
Han, X., Chow, B.Y., Zhou, H., Klapoetke, N.C., Chuong, A., Rajimehr, R., 2011. Front. Syst. Ne. 5 (5), 18.
Häusser, M., 2014. Nat. Methods 11 (10), 1012–1014.
Kampasi, K., English, D.F., Seymour, J., Stark, E., Mckenzie, S., Vöröslakos, M., 2018. Microsyst. Nanoeng. 4 (1).
Kampasi, K., Stark, E., Seymour, J., Na, K., Winful, H.G., Buzsáki, G., 2016. Sci. Rep. 6, 30961.
Kewley, D.T., Hills, M.D., Borkholder, D.A., Opris, I.E., Maluf, N.I., Storment, C.W., 1997. Sens. Actuators A-Phys. 58 (1), 27–35.
Klapoetke, N.C., Murata, Y., Kim, S.S., Pulver, S.R., Birdseybenson, A., Cho, Y.K., 2014. Nat. Methods 11 (9), 338–346.
Lee, J., Ozden, I., Song, Y.K., Nurmikko, A.V., 2015. Nat. Methods 12 (12), 1157–1162.
Liao, Y.F., Tsai, M.L., Yen, C.T., Cheng, C.H., 2011. J. Neurosci. Meth. 195 (2), 211–215.
Liu, D., Gu, X., Zhu, J., Zhang, X., Han, Z., Yan, W., 2014. Science 346 (6208), 458–463.
Madisen, L., Mao, T., Koch, H., Zhuo, J.M., Berenyi, A., Fujisawa, S., 2012. Nat. Neurosci. 15 (5), 793.
Mavoori, J., Jackson, A., Diorio, C., Fetz, E., 2005. J. Neurosci. Methods 148 (1), 71–77.
Miesenböck, G., 2011. Cell Dev. Biol. 27 (1), 731–758.
Nagel, G., Brauner, M., Liewald, J.F., Adeishvili, N., Bamberg, E., Gottschalk, A., 2005. Curr. Biol. 15 (24), 2279–2284.
Nagel, G., Szellas, T., Huhn, W., Kateriya, S., Adeishvili, N., Berthold, P., 2003. P. Natl. Acad. Sci. USA 100 (24), 13940–13945.
Najafi, K., Wise, K.D., Mochizuki, T., 1985. IEEE Trans. Electron Devices 32 (7), 1206–1211.
Norlin, P., Kindlundh, M., Mouroux, A., Yoshida, K., Hofmann, U.G., 2002. J. Micromech. Microeng. 12 (12), 414–419.
Oh, S.W., Harris, J.A., Ng, L., Winslow, B., Cain, N., Mihalas, S., 2014. Nature 508 (7495), 207–214.
Pasupathy, A., Miller, E.K., 2005. Nature 433 (7028), 873.
Patel, P.R., Na, K., Zhang, H., Kozai, T.D.Y., Kotov, N.A., Yoon, E., 2015. J. Neural Eng. 12 (4), 046009.
Patel, P.R., Zhang, H., Robbins, M.T., Nofar, J.B., Marshall, S.P., Kobylarek, M.J., 2016. J. Neural Eng. 13 (6), 066002.
Pisanello, F., Sileo, L., Oldenburg, I.A., Pisanello, M., Martiradonna, L., Assad, J.A., 2014. Neuron 82 (6), 1245.
Schwaerzle, M., Paul, O., Ruther, P., 2017. J. Micromech. Microeng. 27 (6).
Schwaerzle, M., Seidl, K., Schwarz, U.T., Paul, O., Ruther, P., 2013. IEEE, International Conference on MICRO Electro Mechanical Systems, pp. 1029–1032.
Son, Y., Jenny, L.H., Kim, J., Shin, H., Choi, N., Justin, L.C., 2015. Sci. Rep. 5, 15466.
Szarowski, D.H., Andersen, M.D., Retterer, S., Spence, A.J., Isaacson, M., Craighead, H.G., 2003. Brain Res. 983 (1–2), 23.
Wang, M.H., Ji, B.W., Gu, X.W., Guo, Z.J., Wang, X.L., Yang, B., Li, C.Y., Liu, J.Q., 2018. Sens. Actuators B Chem. 264 (1), 100–109.
Watanabe, Y., Funahashi, S., 2004. J. Neurophysiol. 92 (3), 1756–1769.
Wietek, J., Beltramo, R., Scanziani, M., Hegemann, P., Oertner, T.G., Wiegert, J.S., 2015. Sci. Rep. 5.
Williams, J.C., Hippensteel, J.A., Dilgen, J., Shain, W., Kipke, D.R., 2007. J. Neural Eng. 4 (4), 410–423.
Winslow, B.D., Tresco, P.A., 2010. Biomaterials 31 (7), 1558–1567.
Wise, K.D., Angell, J.B., Starr, A., 1970. IEEE Trans. Biomed. Eng. 17, 238–247.
Wu, F., Stark, E., Im, M., Cho, I.J., Yoon, E.S., Buzsáki, G., 2013. J. Neural Eng. 10 (5), 056012.
Xie, K., Fox, G.E., Liu, J., Tsien, J.Z., 2016. Front. Syst. Ne. 10, 8256.
Yizhar, O., Fenno, L.E., Davidson, T.J., Mogri, M., Deisseroth, K., 2011. Neuron 71 (1), 9.
Zemelman, B., Lee, G., Ng, M., Miesenbock, G., 2002. Neuron 33 (1), 15–22.
Zhang, F., Wang, L.P., Brauner, M., Liewald, J.F., Kay, K., Watzke, N., 2007. Nature 446 (7136), 633–639.
Zorzos, A.N., Scholvin, J., Boyden, E.S., Fonstad, C.G., 2012. Opt. Lett. 37 (23), 4841.